Matter, Volume *6*

Supplemental information

Supramolecular filaments for concurrent ACE2 docking and enzymatic activity silencing enable coronavirus capture and infection prevention

Caleb F. Anderson, Qiong Wang, David Stern, Elissa K. Leonard, Boran Sun, Kyle J. Fergie, Chang-yong Choi, Jamie B. Spangler, Jason Villano, Andrew Pekosz, Cory F. Brayton, Hongpeng Jia, and Honggang Cui

Supplemental Items

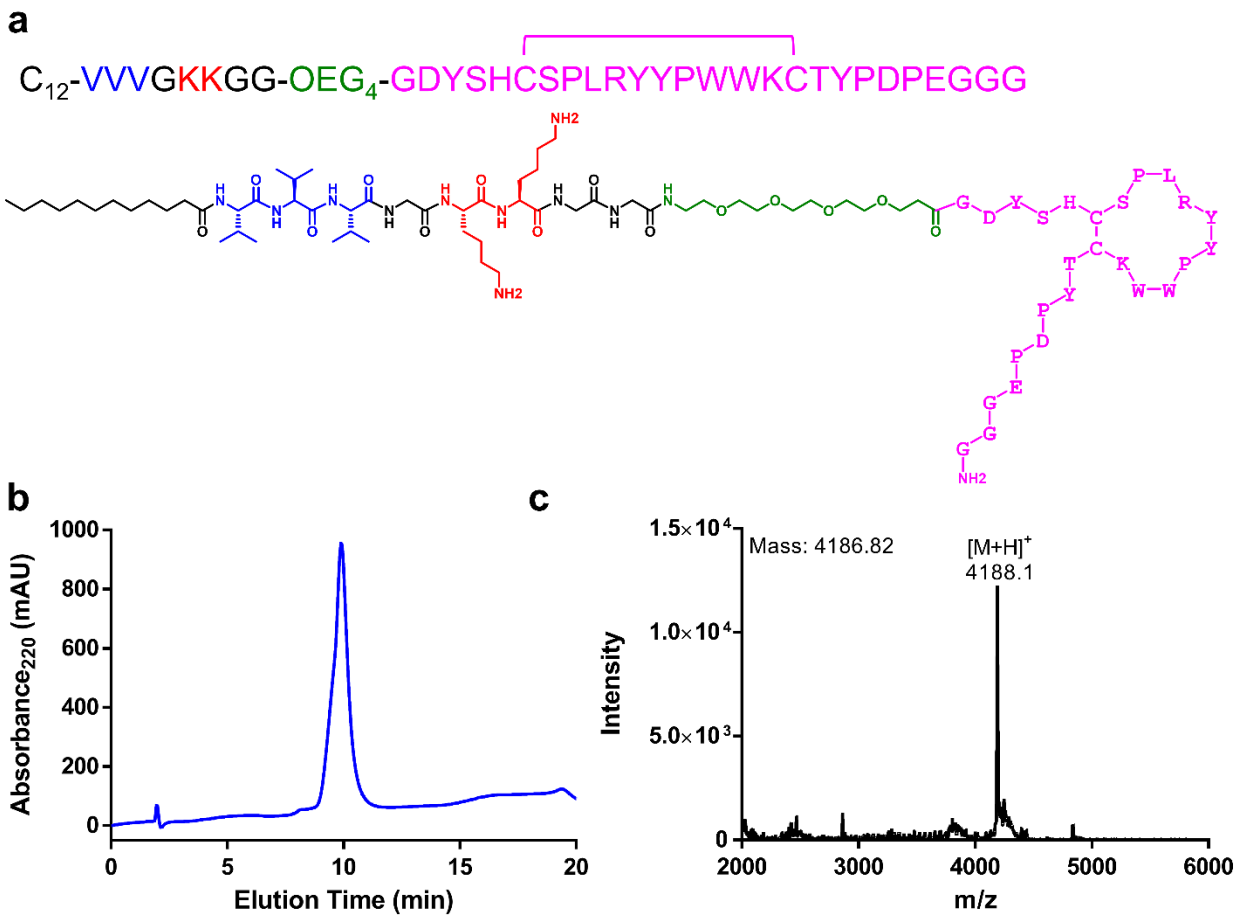

Figure S1. Molecular design and characterization of Ligand PA. (**a**) Full peptide sequence and chemical structure of Ligand, showing full sequence of ACE2-inhibiting peptide ligand, DX600, through which ACE2 specifically binds to the PA molecule. Full chemical structure of Ligand PA is detailed in Figure S21. (**b**) Analytical RP-HPLC chromatogram of Ligand, showing high purity. (**c**) MALDI-ToF mass spectrum of Ligand, where peak at 4188.1 corresponds to $[M+H]^+$ (compared to calculated molecular weight of 4186.82).

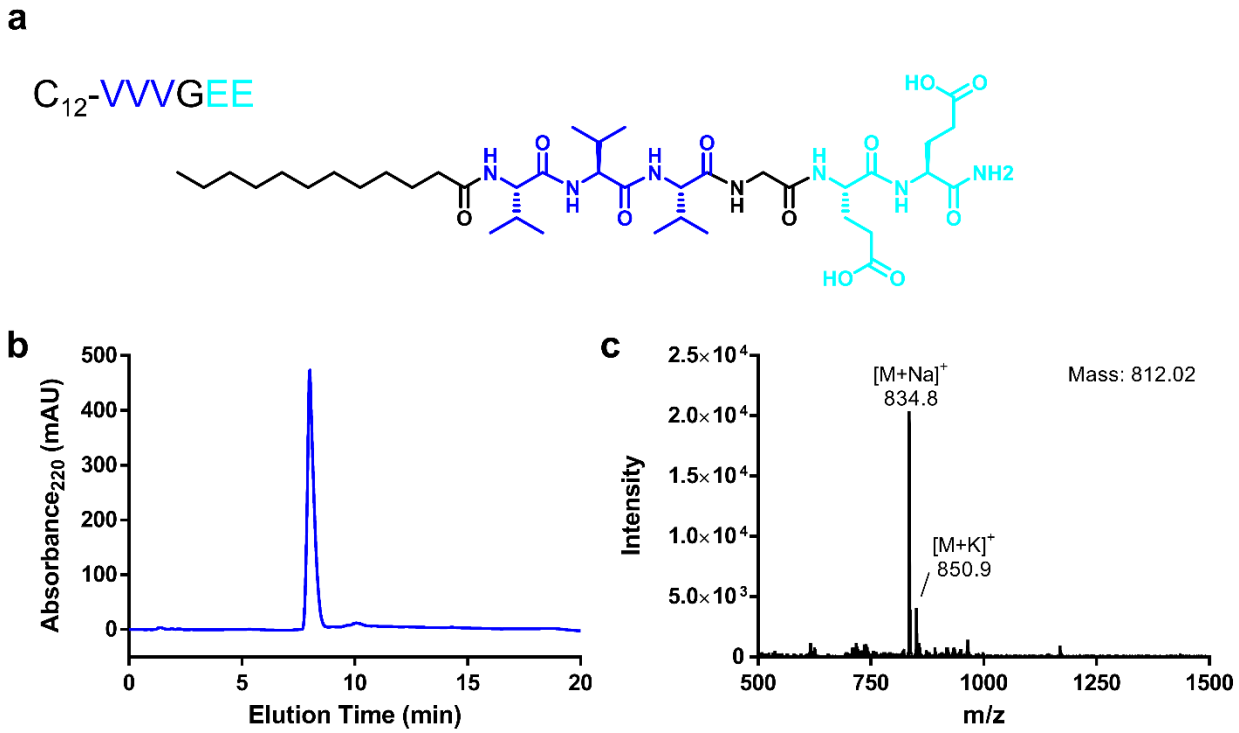

Figure S2. Molecular design and characterization of Filler PA. (**a**) Full peptide sequence and chemical structure of Filler. (**b**) Analytical RP-HPLC chromatogram of Filler, showing high purity. (**c**) MALDI-ToF mass spectrum of Filler, where peaks at 834.8 and 850.9 correspond to $[M+Na]^+$ and $[M+K]^+$, respectively (compared to calculated molecular weight of 812.02).

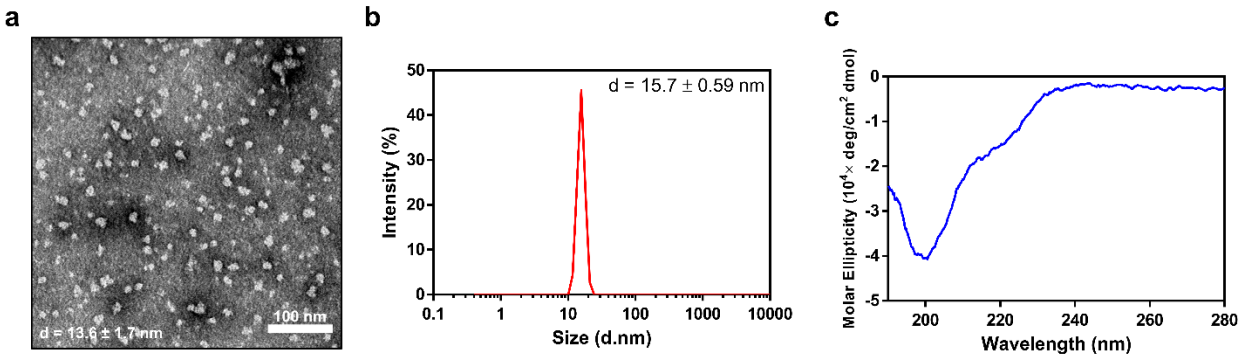

Figure S3. Self-assembly characterization of Ligand PA alone. (**a**) Representative transmission electron microscopy image of Ligand at 200 μM in MilliQ water (pH = 7.4) after aging for 24 h, showing assembly into spherical aggregates. Diameter represented as mean ± SD (n = 35). (**b**) Dynamic light scattering measurement of Ligand at 100 μM in PBS (pH = 7.4) after aging for 24 h, confirming presence of spherical aggregates observed with TEM. Diameter measurement presented as mean ± SD (n = 3). (**c**) Circular dichroism measurement of Ligand spherical aggregates at 100 μM in MilliQ water (pH = 7.4) after aging for 24 h, showing random coil secondary structure as evidenced by negative peak around 200 nm.

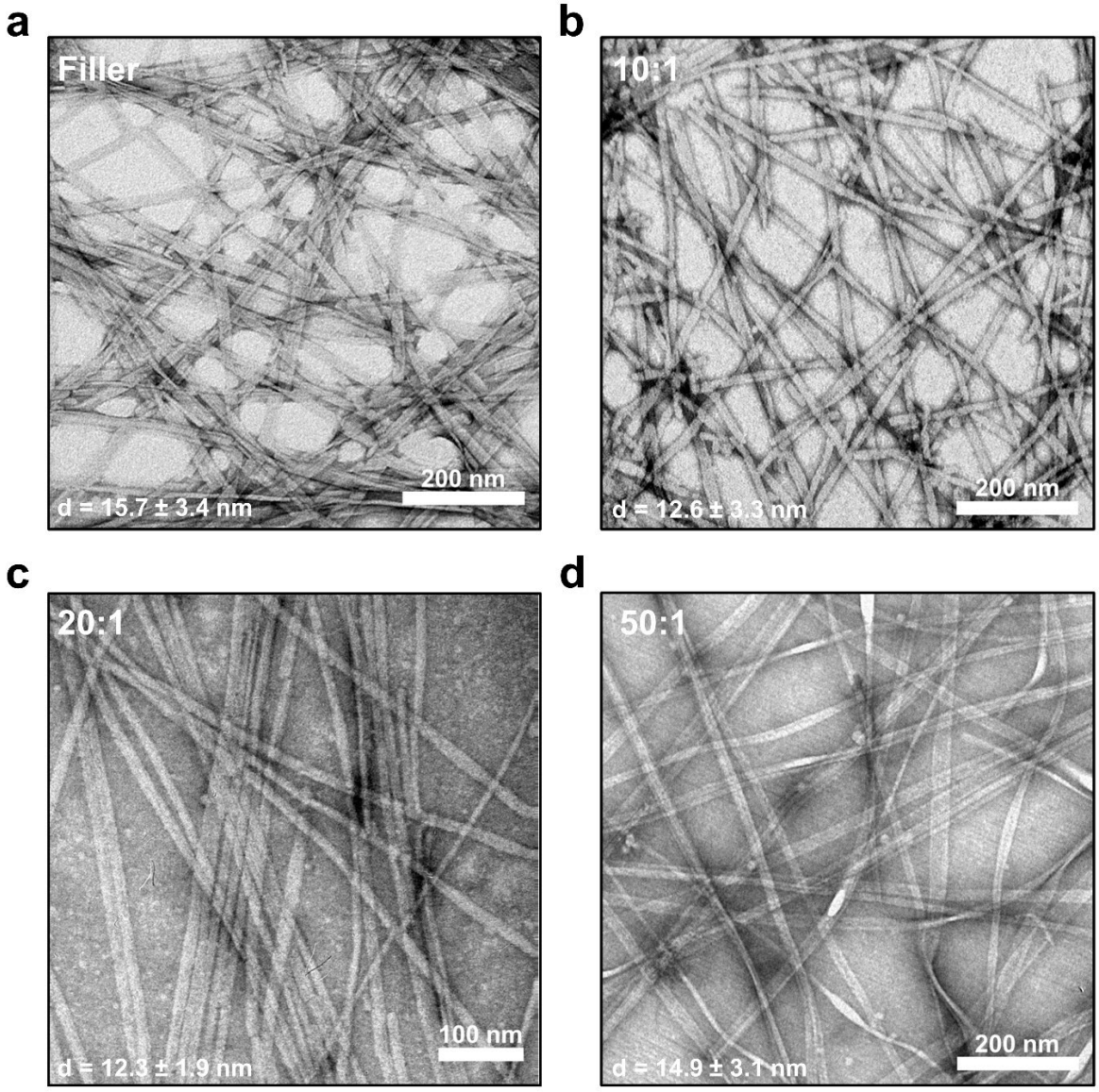

Figure S4. Self-assembly characterization of the co-assembly of Filler and Ligand at varying molar ratios. Representative transmission electron microscopy (TEM) image of (**a**) Filler at 500 μM, in MilliQ water (pH = 7.4) after aging for 24 h, showing assembly into ribbon-like filaments. Diameter represented as mean ± SD (n = 35). Representative TEM image of (**b**) 10:1, (**c**) 20:1, and (**d**) 50:1 molar ratio of Filler:Ligand with 50 μM Ligand in MilliQ water (pH = 7.4) after aging for 24 h, showing co-assembly into ribbon-like filaments for every ratio studied. Diameters represented as mean ± SD (n = 35).

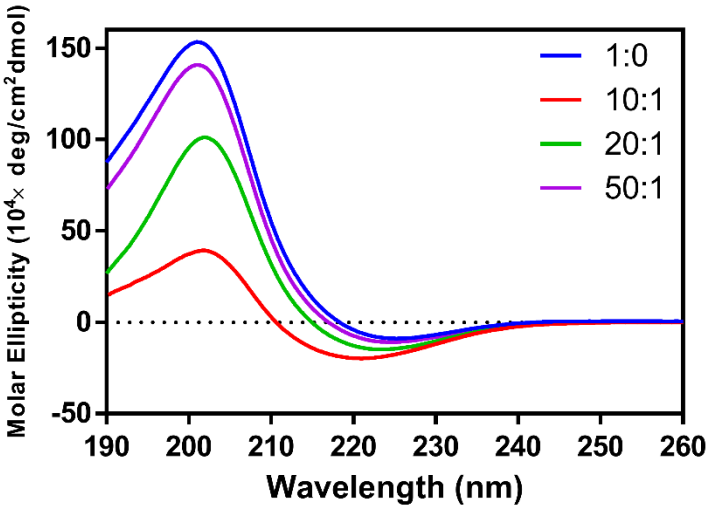

Figure S5. Circular dichroism (CD) spectra of the co-assembly of Filler and Ligand at varying molar ratios, ranging from 1:0 to 50:1 Filler:Ligand. All spectra are representative of samples in MilliQ water at pH = 7.4 after immediate dilution to 100 μM before scanning. The CD spectra of 1:0 shows an intense positive peak around 207 nm and red-shifted negative peak at ~226 nm, which is suggestive of β-turn character in addition to more linear β-sheet character.[1,2] With increasing content of Ligand in the supramolecular structures, the β-turn content decreases and CD spectra represent more typical linear β-sheet character with stronger negative peak at ~220 nm and weaker, blue-shifted positive peak at ~202 nm. Spectrum for each sample represents average of 3 scans.

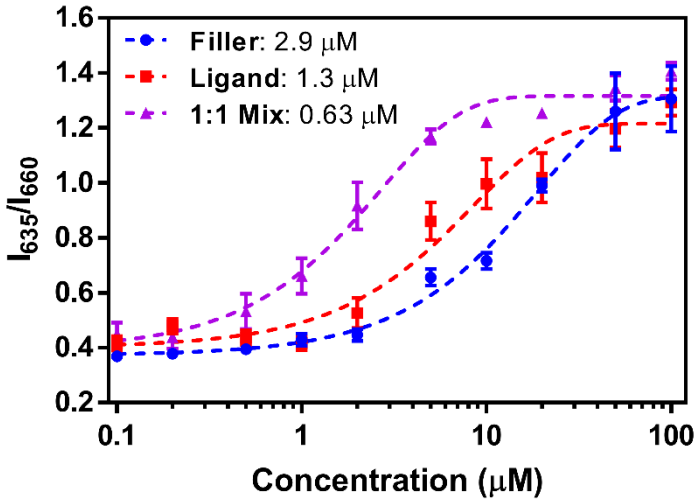

Figure S6. Determination of critical micelle concentration (CMC) for Filler, Ligand, and their co-assembly in MilliQ water (pH = 7.4) using Nile Red assay. The fluorescence intensity maximum is shifted from 660 nm to 635 nm as the Nile Red dye becomes encapsulated within the supramolecular structures of the PAs. The presented CMC values are calculated as the transition point between the two wavelengths. Data are presented as mean ± SD (n = 3).

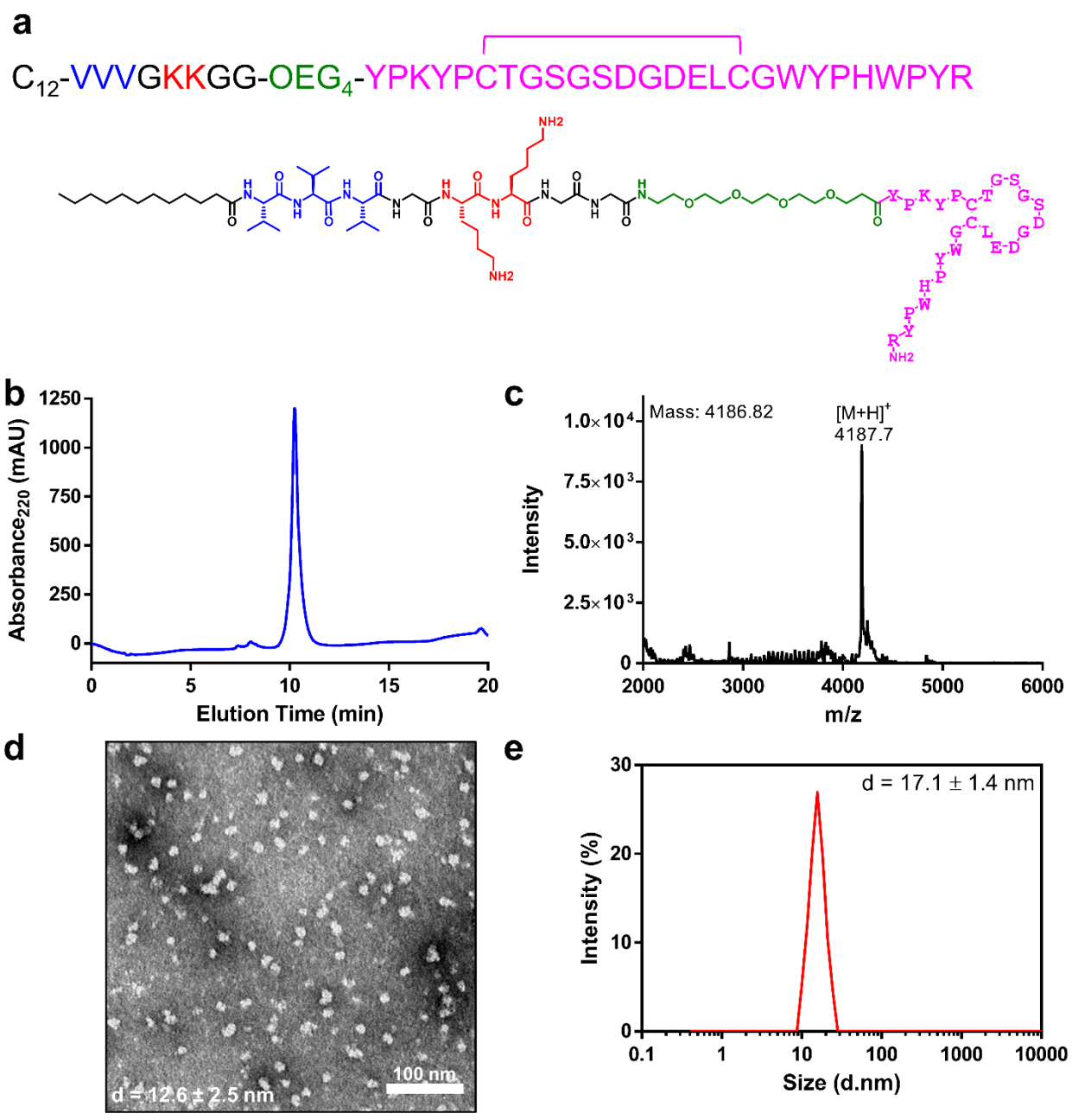

Figure S7. Molecular design, characterization, and self-assembly behavior of sLigand PA. (**a**) Full peptide sequence and chemical structure of sLigand, showing scrambled sequence of ACE2-inhibiting peptide ligand, DX600, where loop is maintained in the same position, but the amino acid sequence was randomly shuffled otherwise. (**b**) Analytical RP-HPLC chromatogram of sLigand, showing high purity. (**c**) MALDI-ToF mass spectrum of sLigand, where peak at 4187.7 corresponds to $[M+H]^+$ (compared to calculated molecular weight of 4186.82). (**d**) Representative transmission electron microscopy image of sLigand at 200 μM in MilliQ water (pH = 7.4) after aging for 24 h, showing assembly into spherical aggregates. Diameter represented as mean ± SD (n = 35). (**e**) Dynamic light scattering measurement of sLigand at 100 μM in PBS (pH = 7.4) after aging for 24 h, confirming presence of spherical aggregates observed with TEM. Diameter measurement presented as mean ± SD (n = 3).

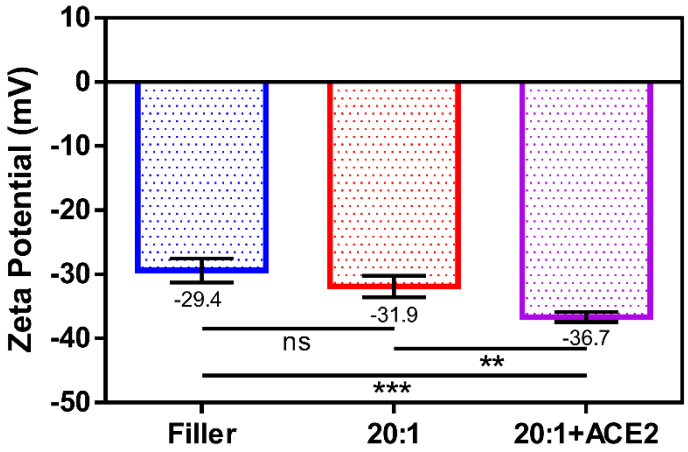

Figure S8. Zeta potential measurements of Filler alone and ACE2-docking filaments (20:1 molar ratio Filler:Ligand) before and after ACE2 addition. Filament zeta potential is negligibly impacted by incorporation of Ligand, emphasizing role of Filler in regulating surface charge. Large drop in zeta potential after addition of ACE2 suggests complexation at the surface of the supramolecular filaments. Data are presented as mean ± SD (ns $p > 0.5$, ** $p < 0.01$, *** $p < 0.001$, one-way ANOVA with Tukey's post hoc test, n = 3).

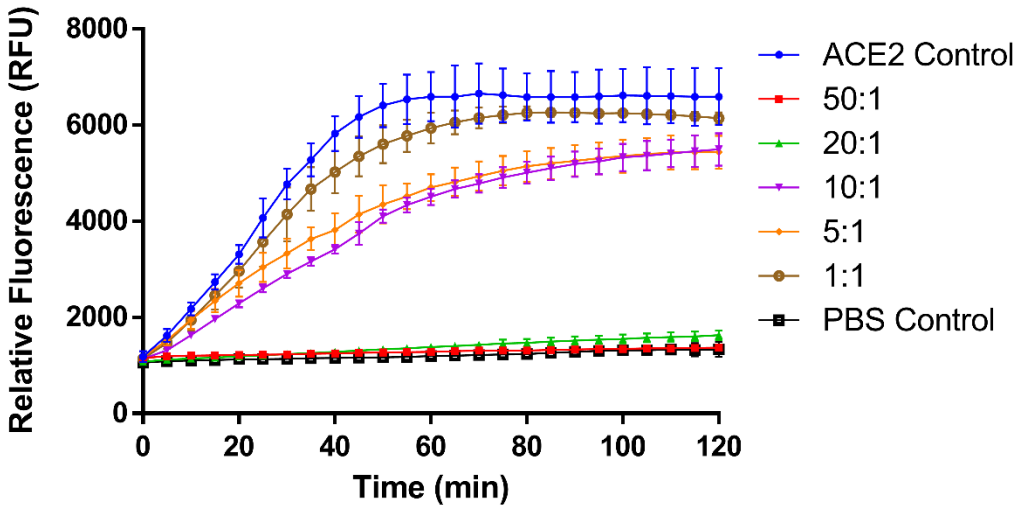

Figure S9. Kinetic measurement of evolved fluorescence intensity of activity probe by ACE2 cleavage in the presence of ACE2-docking filaments. The concentration of Filler within the filaments is varied while holding Ligand and ACE2 concentration constant, showing greater inhibition of ACE2 with increased spacing. Data presented as mean ± SD (n = 3).

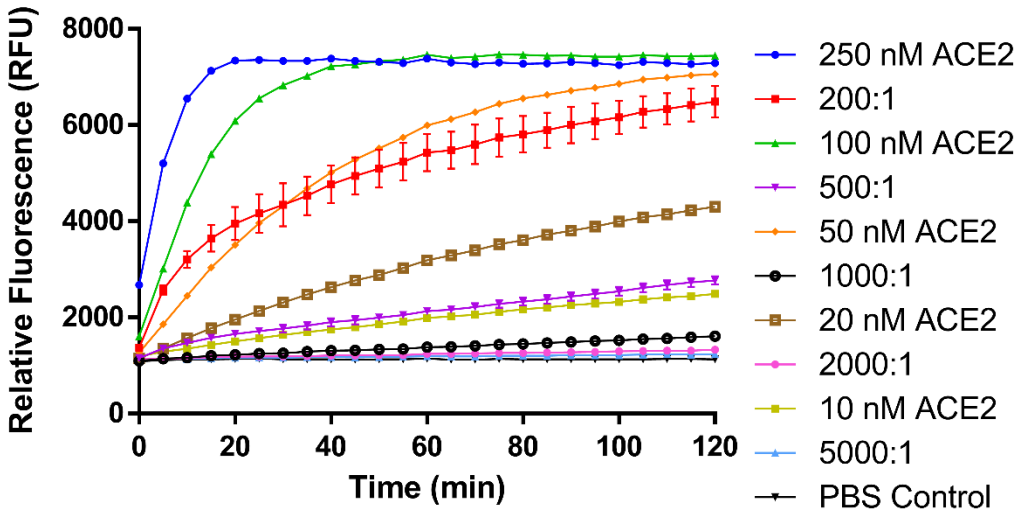

Figure S10. Kinetic measurement of evolved fluorescence intensity of activity probe by ACE2 cleavage in the presence of ACE2-docking filaments. The molar ratio of Filler to Ligand is held constant (20:1) while the Ligand:enzyme ratio is varied, showing greater inhibition with greater Ligand to ACE2 ratios. Data presented as mean ± SD (n = 3).

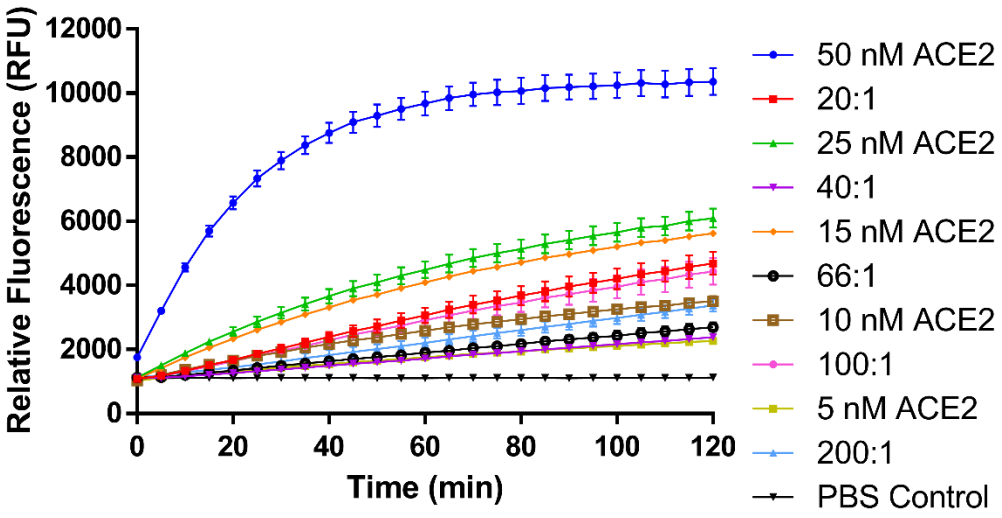

Figure S11. Kinetic measurement of evolved fluorescence intensity of activity probe by ACE2 cleavage in the presence of ACE2-docking filaments. Both the concentration of Filler and the Ligand:enzyme ratio are fixed while the concentration of Ligand is varied, showing greater inhibition of ACE2 with increasing Ligand concentration. Data presented as mean ± SD (n = 3).

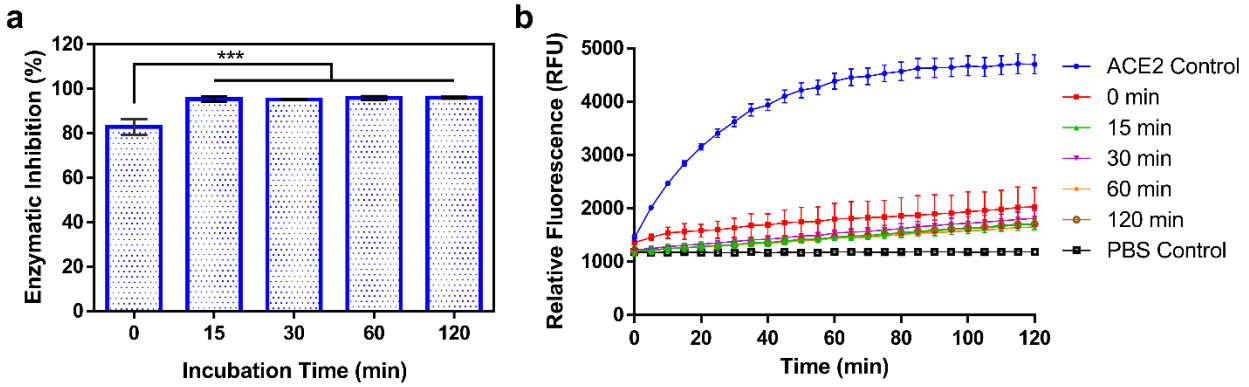

Figure S12. Influence of incubation time on docking efficiency of ACE2 to ACE2-docking filament surfaces. (**a**) Enzymatic inhibition (calculated based on relative reaction initial velocities compared to free ACE2) of ACE2 after incubation with ACE2-docking filaments for set time before assessment with activity assay, showing maximum docking achieved after 15 min. Data presented as mean ± SD (***$p < 0.001$, ns $p > 0.05$ amongst groups 15 min and later; one-way ANOVA with Tukey's post hoc test, n = 3). (**b**) Kinetic measurement of evolved fluorescence of activity probe by ACE2 cleavage in the presence of ACE2-docking filaments after incubation for varied times before assessment with activity assay, showing a minimum of 15 min is required to achieve maximum inhibition of ACE2 activity. Data presented as mean ± SD (n = 3).

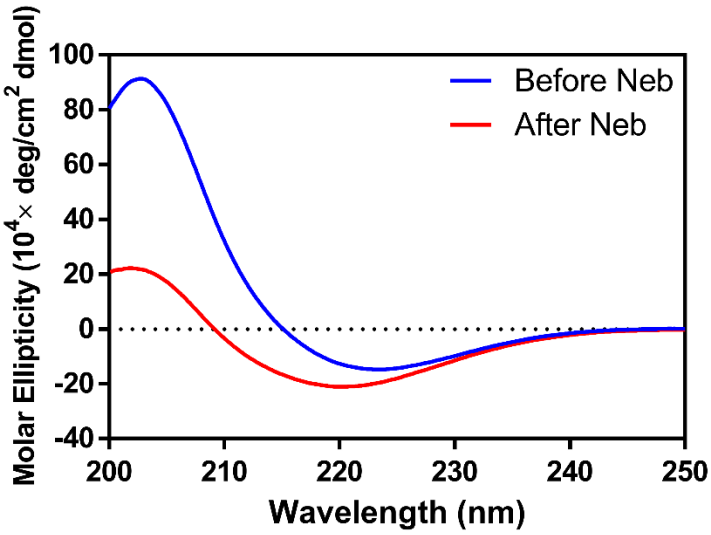

Figure S13. Circular dichroism (CD) spectra of **fACE2** before and after nebulization (1 mM in PBS at pH = 7.4 with immediate dilution to 100 μM before running sample), showing retention of β-sheet character (negative peaks around 220 nm) after nebulization but also a reduction in signal intensity reflective of disrupted hydrogen-bonding. Spectra represent average of 3 scans.

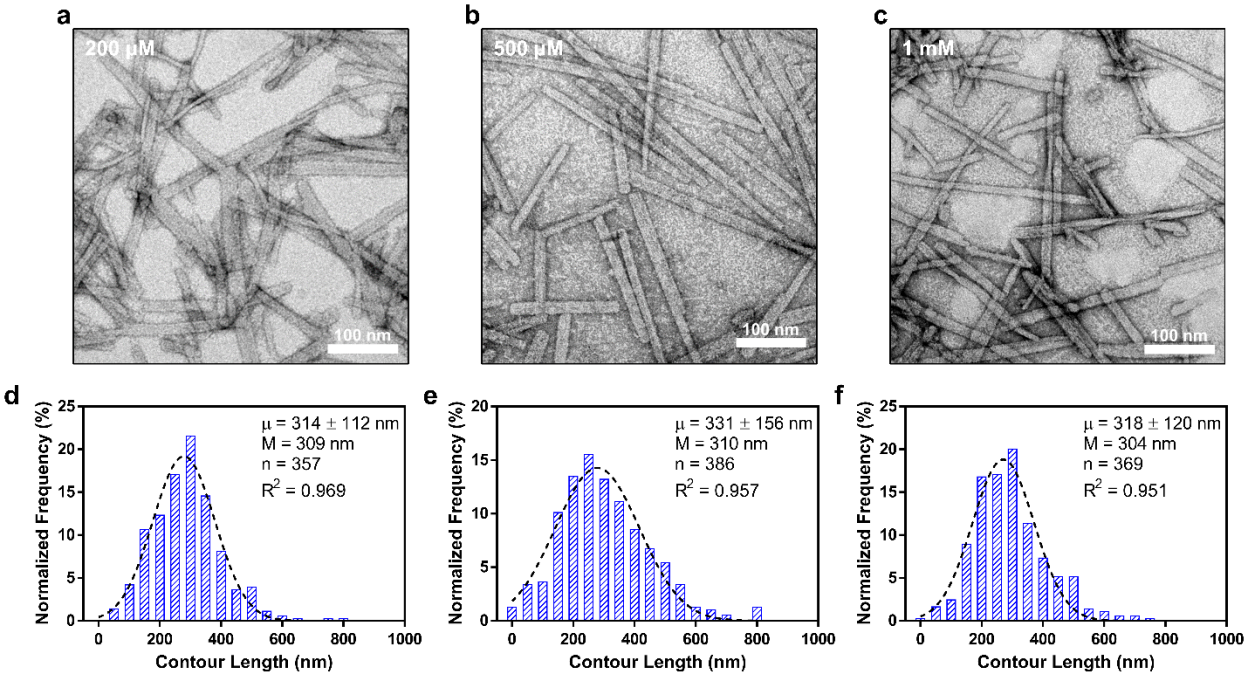

Figure S14. Post-nebulization filament fragmentation of various formulation concentrations of **fACE2** in PBS (pH = 7.4). Representative transmission electron microscopy images of **fACE2** at (**a**) 200 µM, (**b**) 500 µM, and (**c**) 1 mM after nebulization, showing reduced filament length. Population size distributions for the contour lengths of observed filaments after jet nebulization for each formulation concentration of **fACE2** (20 bins, 50 nm each) from TEM images, where µ represents average contour length given as mean ± SD alongside median (M) measured length: (**d**) 200 µM (n = 357 analyzed filaments), (**e**) 500 µM (n = 386 analyzed filaments), and (**f**) 1 mM (n = 369 analyzed filaments). Dotted lines represent fit of data to a Gaussian distribution. For average contour length of each starting concentration, ns $p > 0.05$ by one-way ANOVA with Tukey's post hoc test, highlighting the similarity of the size distributions.

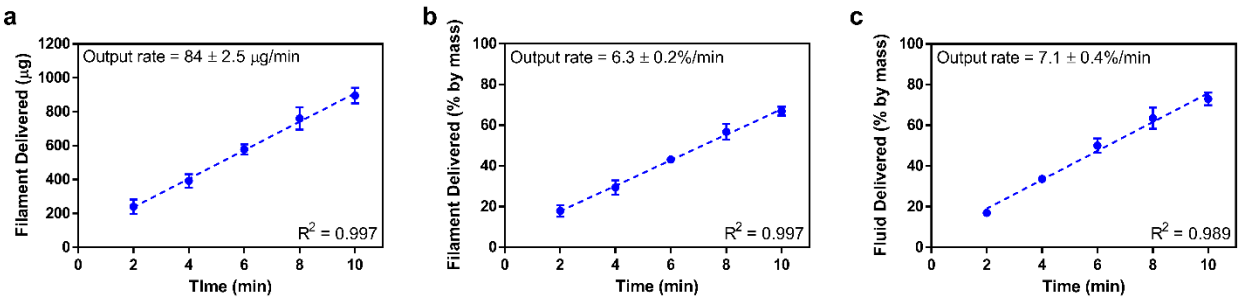

Figure S15. Release profiles of **fACE2** from a jet nebulizer over the course of a 10 min nebulization event (500 µM formulation in PBS at pH = 7.4). Release of **fACE2** by (**a**) total mass emitted (µg), (**b**) fraction of loaded dose (% by mass), and (**c**) weight of formulation fluid (% by mass), highlighting linear profile. Data presented as mean ± SD (n = 3); dashed lines represent results of linear regression analysis. For output rates of filament mass and fluid mass (%), ns $p > 0.05$ by two-tailed unpaired *t*-test with Welch's correction, though slightly lower output rate of filaments may reflect heterogeneity in aerosol droplet concentration over the course of a nebulization event.

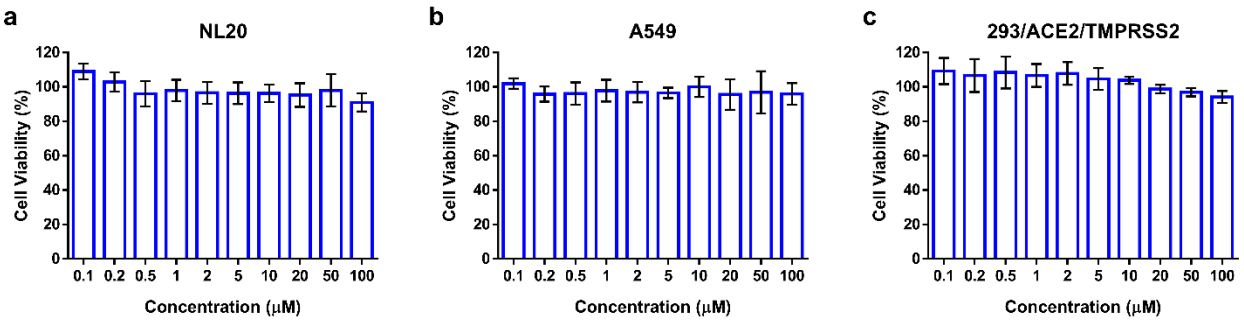

Figure S16. Cytotoxicity of ACE2-docking filaments after 48 h incubation concentrations (ranging from 0.1 to 100 μM) for (**a**) NL20, (**b**) A549, and (**c**) 293/ACE2/TMPRSS2 cells lines as determined by MTT assay. Data presented as mean ± SD (n = 3 independent experiments).

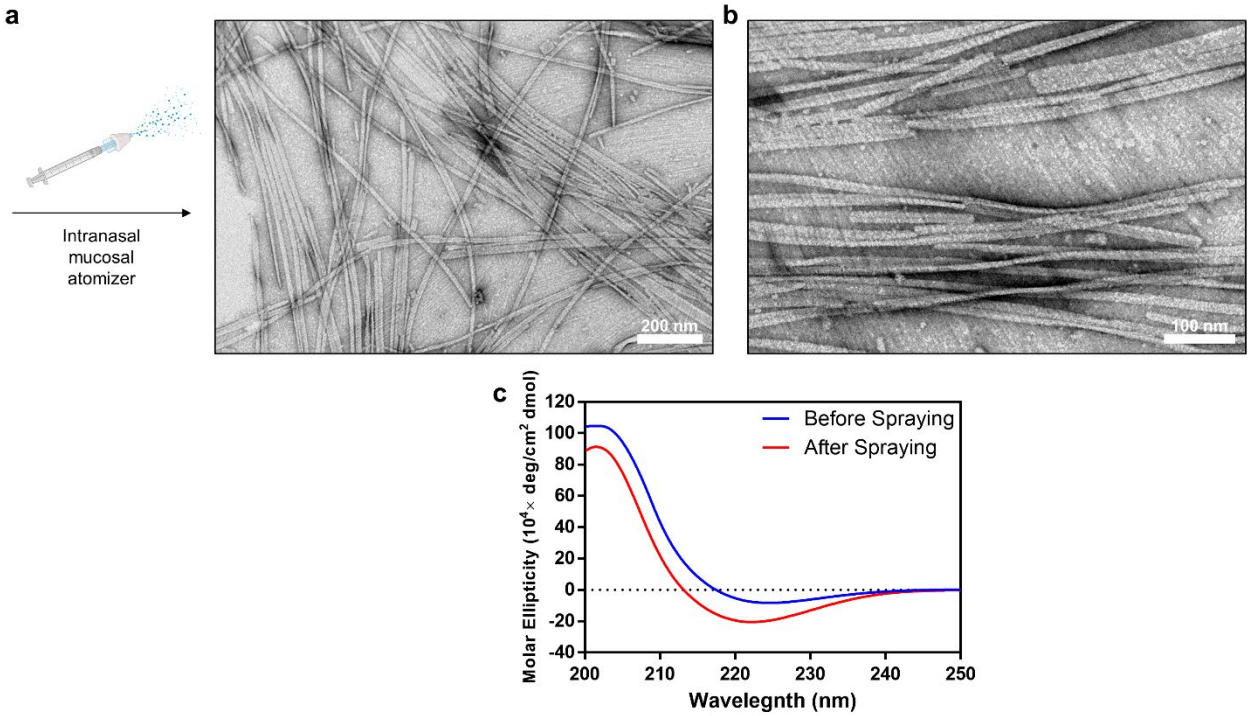

Figure S17. Filament characterization of **fACE2** after administration with an intranasal mucosal atomizer. Representative (**a**) low- and (**b**) high-magnification transmission electron microscopy images of **fACE2** (500 μM in PBS, pH = 7.4) post-atomization, showing instances of filament fragmentation and alignment, likely due to shear forces. (**c**) Circular dichroism (CD) spectra of **fACE2** before and after atomization (500 μM in PBS at pH = 7.4 with immediate dilution to 100 μM before running sample), showing retention of β-sheet character (negative peaks around 220 nm) after nebulization but also a reduction in signal intensity reflective of disrupted hydrogen-bonding. Spectra represent average of 3 scans.

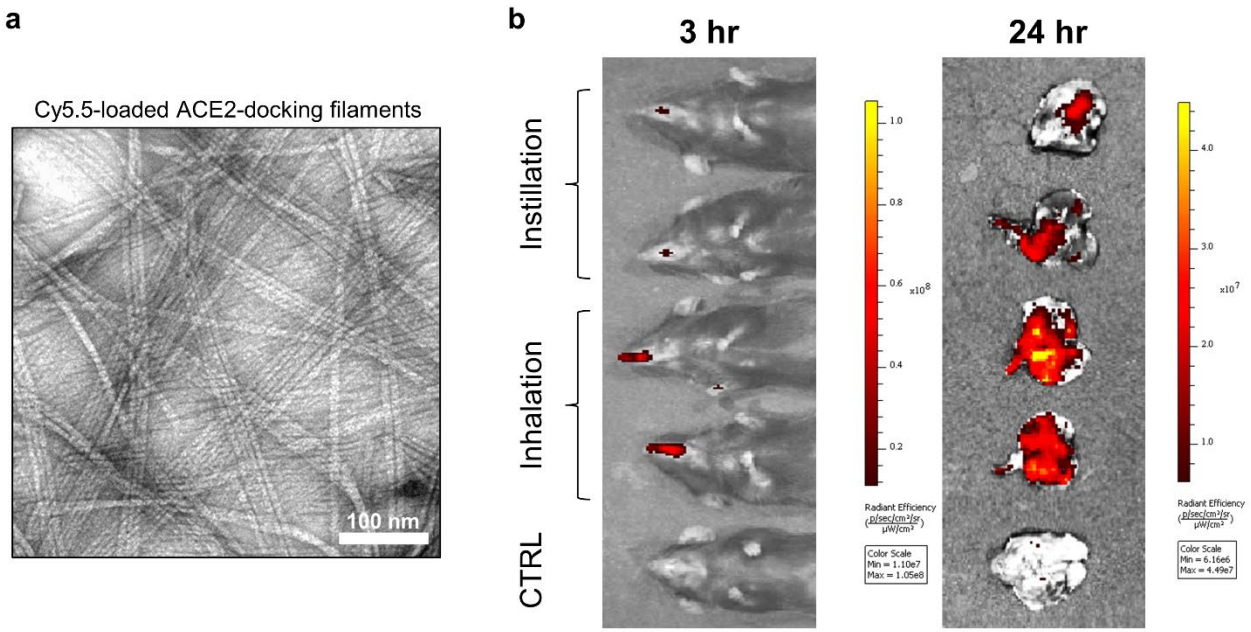

Figure S18. *In vivo* lung distribution study of ACE2-docking filaments in K18-hACE2 mice after inhalation administration. (**a**) Representative transmission electron microscopy image of near-infrared dye Cyanine 5.5-loaded ACE2-docking filaments (500 μM in PBS, pH = 7.4) used for visualizing filament distribution. (**b**) In Vivo Imaging System (IVIS) fluorescence imaging of K18-hACE2 mice after administration of atomized Cy5.5-loaded ACE2-docking filaments (in PBS, 10 nM equivalent ACE2 dose (molar ratio 20:1 Filler:Ligand filaments, 200 μM)) either via intratracheal instillation or intranasal inhalation (control = intranasal inhalation of PBS only). Images on left shows retention of filaments in nasal cavity of mice 3 h post-administration. Lungs harvested from mice 24 h post-administration of filaments shows strong fluorescence signal from filaments throughout lung tissues, suggesting enhanced retention (n = 2 mice per group, 1 control). Experiments were repeated twice with similar results.

Note S1 on Figure S18:

The observed differences in filament retention and distribution between the intranasal inhalation and intratracheal instillation groups can likely be attributed to the differences in these routes of administration. With intratracheal instillation, intubated mice receive filaments directly to the lungs, bypassing the upper respiratory tract and delivering a bolus dose. This can lead to heterogenous distribution patterns of lung retention. In contrast, intranasal inhalation delivers filaments through the physiological route, where breathing filament-bearing droplets leads to deeper and more spread distribution within the lungs. A greater portion of lung tissue is observed to contain fluorescence signal for the inhalation group, whereas the instillation group shows fluorescence localized closer to the trachea.[3-5]

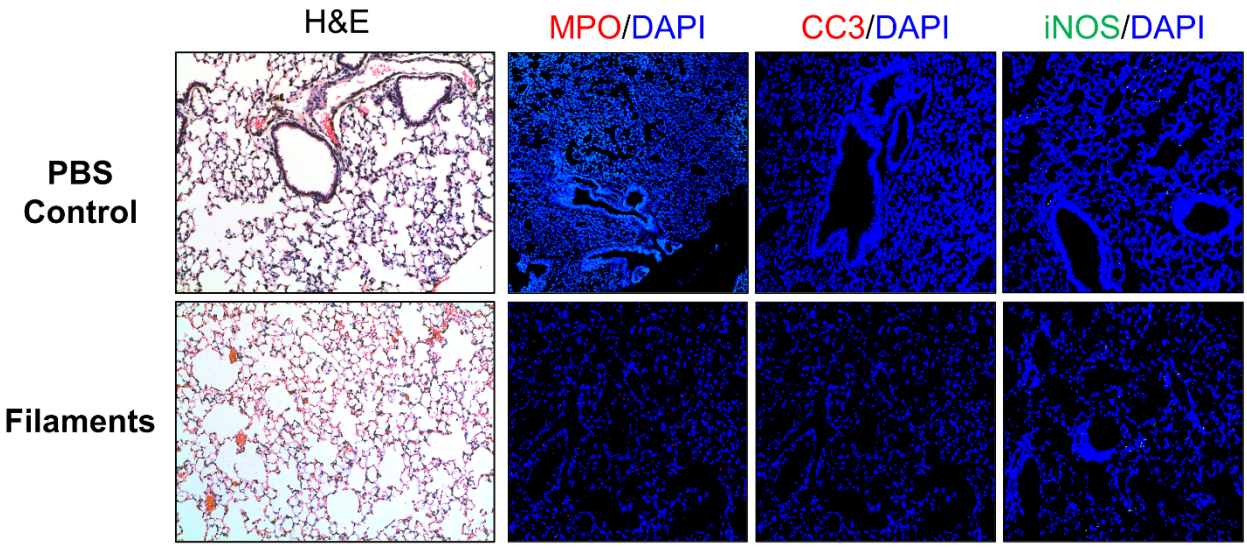

Figure S19. Histology of lung tissue sections of K18-hACE2 mice 24 h after administration of atomized Cy5.5-loaded ACE2-docking filaments (in PBS, 10 nM ACE2 equivalent dose (molar ratio 20:1 Filler:Ligand filaments, 200 μM)) via intranasal inhalation. Compared to PBS-only control, hematoxylin and eosin (H&E) staining and immunofluorescence show no obvious sign of lung cell apoptosis, inflammation, or neutrophil infiltration from treatment with ACE2-docking filaments, suggesting filaments are relatively biocompatible and safe delivery vehicles for ACE2 (neutrophil invasion, myeloperoxidase (anti-MPO antibody), red; apoptosis marker, cleaved-caspase 3 (anti-CC3 antibody), red; pro-inflammatory cytokine production, inducible nitric oxide synthase (anti-iNOS antibody), green; cell nuclei, DAPI, blue). Experiments were repeated twice with similar results.

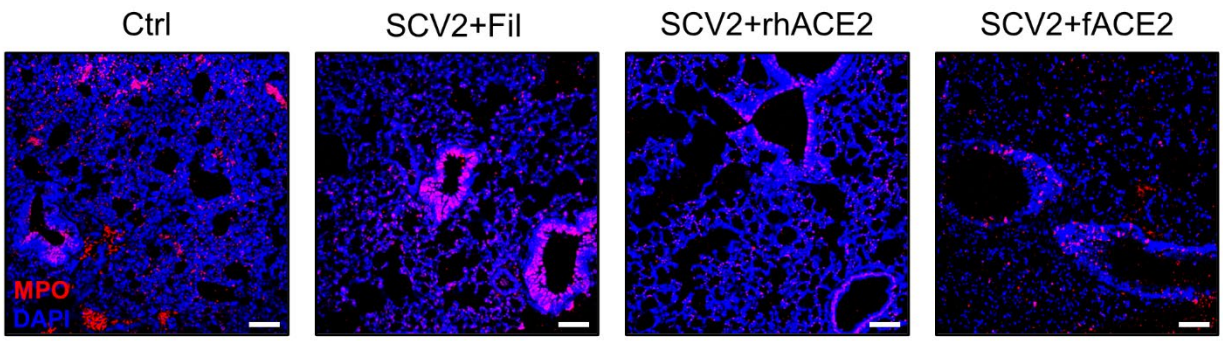

Figure S20. Immunofluorescence staining of harvested mouse lung tissue sections after treatment and SARS-CoV-2 inoculation, assessing neutrophil infiltration. Neutrophil invasion is markedly decreased with treatment with fACE2, indicating alleviated lung inflammation and related pathology (myeloperoxidase (anti-MPO antibody), red; cell nuclei (DAPI), blue). Scale bars represent 50 μm.

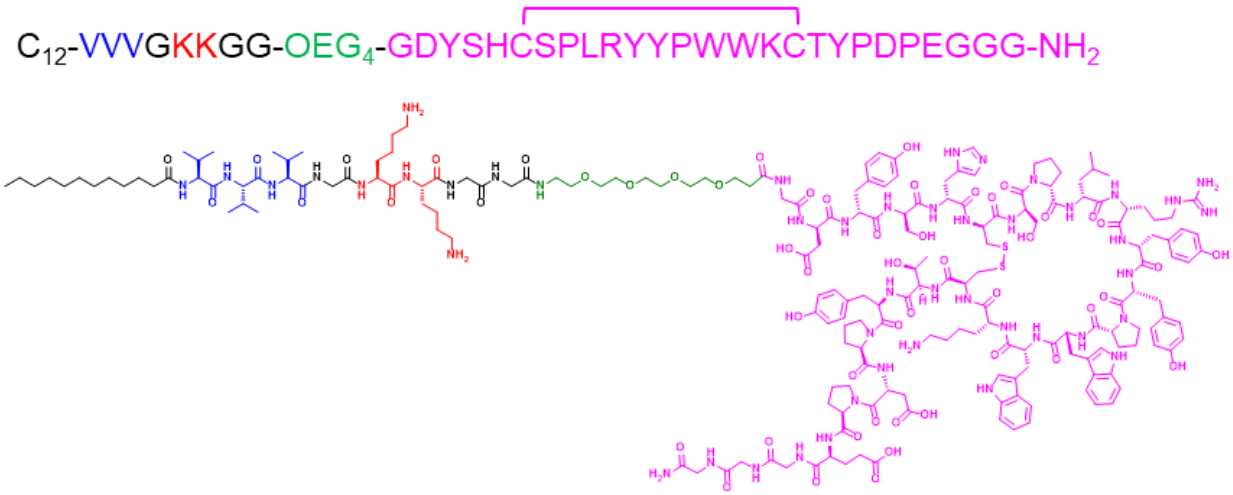

Figure S21. Full chemical structure of the Ligand PA design.

Supplemental Experimental Procedures

Peptide amphiphile synthesis and purification

All peptide amphiphiles (PAs) studied were synthesized using standard 9-fluorenylmethoxycarbonyl (Fmoc) solid phase peptide synthesis techniques. All three PAs (Filler, Ligand, sLigand) were synthesized onto Rink amide 4-methylbenzhydrylamine (MBHA) resin (100-200 mesh, 0.53 mmol/g). All Fmoc deprotections were performed with 20% 4-methylpiperidine in *N*,*N*-dimethylformamide (DMF) for 15 minutes, repeated once. After Fmoc removal, each amino acid coupling was performed at a 4:4:6 molar ratio of the Fmoc-protected amino acid, O-benzotrizole-*N*,*N*,*N*',*N*'-tetramethyluronium hexafluorophosphate (HBTU), and *N*,*N*-diisopropylethylamine (DIEA) in DMF and shook for 2 h for the coupling reaction. For Ligand and sLigand molecules, Fmoc-PEG_4-COOH was conjugated to peptide chain at a molar ratio of 2:2:3 to resin of Fmoc-PEG_4-COOH, HBTU, and DIEA in DMF and shaken for 24 h. After final amino acid conjugation and Fmoc deprotection, lauric acid (C_{12} alkyl chain) was coupled to the peptide in a 4:4:6 molar ratio to resin of lauric acid, HBTU, and DIEA in DMF and shaken overnight. For Ligand and sLigand molecules, Acm deprotection and disulfide bond formation (from Cys(Acm) residues of the DX600 peptide ligand segment of the design) was conducted with thallium trifluoroacetate (2 equivalents) in DMF and swirled with resin on ice for 2 h; resin was subsequently washed with methanol (MeOH), DMF, and then MeOH again. Completed PAs were cleaved from their resin by addition of a 10 mL mixture of 95% v/v trifluoroacetic acid (TFA), 2.5% v/v triisopropylsilane (TIS), and 2.5% v/v water and shaken for 3 h. After cleavage, the TFA solution was collected and excess TFA removed via evaporation, and subsequently the product was precipitated with cold diethyl ether and then dried under vacuum overnight.

Each crude PA solid was dissolved in a water and acetonitrile (ACN) mixture containing 0.1% v/v TFA for Ligand and sLigand molecules and 0.1% v/v ammonium hydroxide (NH_4OH) for Filler. A Varian ProStar Model 325 (Agilent Technologies, Santa Clara, CA) reverse-phase high performance liquid chromatography (RP-HPLC) was employed to purify the PA molecules using mobile phases of water and ACN at matching acidic or basic phase. PAs were separated from impurities by preparative RP-HPLC using a Varian PLRP-S column (C_{18}, 100 Å, 10 µm, 150 × 25 mm) with a flow rate of 20 mL/min, 10 mL injections, and monitoring at 220 nm for peptide absorbance for all molecules. For Filler, the eluent gradient was run linearly from 30% to 45% ACN over 20 min, and for Ligand and sLigand, the gradient was run linearly from 25% to 55% ACN over 30 min. The collected fractions were analyzed by matrix-assisted laser desorption/ionization time of flight (MALDI-ToF) mass spectrometry to isolate fractions containing the molecules of interest. Correct fractions were combined, and excess ACN was removed via rotary evaporation. Samples were then lyophilized using a FreeZone -105°C 4.5L freeze dryer (Labconco, Kansas City, MO). Re-characterization of the purified PA powders were conducted by analytical RP-HPLC and MALDI-ToF. Product purity was assessed with analytical RP-HPLC using a Varian Pursuit XRs column (C_{18}, 5 µm, 150 × 4.6 mm) with a flow rate of 1 mL/min, 20 µL injections, and monitoring at 220 nm. Purity was assessed with a linear gradient of 5% to 95% ACN over 15 min, where area under the curve (AUC) of the PA peak relative to total AUC of all peaks was used to confirm purity greater than 95% (purity data for each molecule shown in **Figures S1, S2, S7**). The redissolved PAs were calibrated, aliquoted into cryo-vials, re-lyophilized, and stored at -20°C freezer for future use.[6-8]

MALDI-ToF Mass Spectroscopy

Matrix-assisted laser desorption/ionization time of flight (MALDI-ToF) mass spectroscopy was used to analyze the molecular weights for all synthesized PA molecules with a BrukerAutoflex III MALDI-ToF instrument (Bruker, Billerica, MA). Samples were prepared by first depositing a 2 µL droplet of sinapic acid matrix solution (10 mg/mL in 1:1 v/v water:ACN with 0.05% TFA; Sigma-Aldrich) onto an MTP 384 ground steel target plate (Bruker, Billerica, MA). The matrix was allowed to dry for 5-10 min, and then 1 µL of aqueous PA solution was added to the corresponding spot of dried matrix followed by the immediate addition of 1 µL of matrix solution and mixed. The spots were allowed to dry for 10-20 min before analyzing on the instrument, where samples were irradiated with a 355 nm UV laser and analyzed in the reflectron mode. Representative MALDI-ToF mass spectra for each of the PAs studied are shown in **Figures S1, S2, S7**.

Dynamic Light Scattering (DLS)

Spherical micelle/aggregate solutions of Ligand and sLigand dissolved in PBS at pH = 7.4 were diluted to 100 μM and placed in a UV-transparent disposable cuvettes (0.5 mL, 45 × 12 mm, special plastic, Sarstedt, Nümbrecht, Germany). Samples were analyzed on a Malvern Zetasizer Nano-ZS ZEN3600 (Malvern Panalytical) at 25°C. Three runs were collected for each sample (10 scans/measurement) and averaged.

Circular Dichroism (CD)

Solutions of the supramolecular systems were diluted to 100 μM, added to a 1 mm path length quartz UV-Vis absorption cell (Thermo Fisher Scientific, Pittsburgh, PA), and then analyzed with a Jasco J-710 spectropolarimeter (JASCO, Easton, MD). Each sample was analyzed by three repeated scans from wavelengths of 190 to 300 nm (for samples in water) or from 200 to 300 nm (for samples in PBS). The high tension (HT) values were monitored during run collection (ranging from 200 to 600 V) to ensure no scattering artifacts were present in the representative spectra. A background spectrum (water or PBS) was obtained and subtracted from sample spectra. All obtained spectra were averaged over 3 scans and converted from ellipticity (mdeg) to molar ellipticity ($deg \cdot cm^2 \cdot dmol^{-1}$). For nebulized samples, sample concentration post-nebulization was determined using a standard curve derived from analytical HPLC runs to account for solvent evaporation that may occur during aerosol formation.

Critical Micelle Concentration (CMC) Measurements

Using a Nile Red assay, the CMC of each PA monomer (Filler and Ligand) and their co-assembly (1:1 molar ratio) was determined. Nile Red dye intensely fluoresces within hydrophobic environments but is strongly quenched and red-shifted in aqueous environments. Thus, when mixed with PAs at a concentration exceeding the CMC, Nile Red will embed within the hydrophobic core and emit a strong fluorescence signal. A 500 μM stock solution of Nile Red was prepared in acetone, and 10 μL of the stock was added to microcentrifuge tubes. Acetone was evaporated off in the dark. Solutions of the samples (500 μL, water) were added to the tubes at varied concentrations and were aged for 2 days in the dark at room temperature. Samples were added to a quartz micro fluorometer cell (0.7 mL, 10 mm pathlength, Starna Cells, Atascadero, CA), and at an excitation wavelength of 550 nm, five parallel emission spectra were recorded at a wavelength range of 580 to 720 nm on a Duetta UV-Vis-NIR spectrofluorometer (HORIBA Scientific). The emission intensity ratio for each run at 635 nm (emission maximum of Nile Red in a hydrophobic environment) to 660 nm (emission maximum of Nile Red in a hydrophilic environment) was plotted against tested concentrations to obtain a transition curve from which CMC was determined.

Bio-Layer Interferometry (BLI)

Biotinylated human ACE2 (NP_068576.1, Sino Biological) was immobilized to streptavidin-coated tips (Pall Life Sciences) for analysis on an Octet Red96 bio-layer interferometry (BLI) instrument (Sartorius). Less than 5 signal units (nm) of ACE2 was immobilized to minimize mass transfer effects. PBSA (PBS pH 7.2 containing 1% BSA) was used for all dilutions and as dissociation buffer. Tips were exposed to serial dilutions of Ligand PA and sLigand PA in a 96-well plate for 300 s. Dissociation was then measured for 150 s. Surface regeneration for all interactions was conducted using 15 s exposure to 0.1 M glycine pH 3.0 solution. Normalized equilibrium binding curves were obtained by plotting the response value at the end of the association phase for each sample dilution, dividing by the molecular weight of each ligand, and normalizing to the maximum value. Equilibrium binding curves were fitted and K_D values determined using GraphPad Prism data analysis software v9.0, assuming all binding interactions to be first order. Experiments were performed twice with similar results.

Zeta Potential Measurements

All zeta potential measurements were conducted for samples in PBS (pH = 7.4) at 25°C. Samples were added to a disposable folded capillary zeta cell (DTS1070, Malvern Panalytical) and analyzed using a Malvern Zetasizer Nano-ZS ZEN3600 (Malvern Panalytical). For analysis of mixtures, ACE2 was added

to solutions of Ligand, sLigand, and 20:1 docking filaments (molar ratio of Filler:Ligand) at an equal volume, such that a final concentration of 50 nM ACE2 was achieved, alongside 50 μM Ligand or sLigand. Three repeated runs were performed for each sample (20 measurements/run) and then averaged. The intensity-averaged zeta potential for mixtures of samples was calculated based on the average derived count rate and zeta potential measured for the individual components and their respective volume fractions after mixing assuming no interaction. This theoretical value was compared to measured experimental values of the systems after ACE2 addition to invalidate the "no interaction" assumption; these calculations were conducted only for Ligand and sLigand spherical aggregates with ACE2, since filaments are anisotropic and more polydisperse and Zetasizer software uses models for fitting best suited to spherical particles.[9,10]

Intensity-averaged zeta potential: ζ_{AB}
For a mixture of 2 components: component A (volume fraction, α; scattering intensity/derived count rate, int_A; zeta potential, ζ_A) and component B (volume fraction, β; scattering intensity/derived count rate, int_B; zeta potential, ζ_B)

$$\alpha + \beta = 1$$

$$\zeta_{AB} = \frac{\alpha \cdot int_A \cdot \zeta_A + \beta \cdot int_B \cdot \zeta_B}{\alpha \cdot int_A + \beta \cdot int_B}$$

For ACE2 + Ligand (equal volume fractions): calculated ζ_{AB} = -17.6 mV, measured -25.1 mV
For ACE2 + sLigand (equal volume fractions): calculated ζ_{AB} = -19.0 mV, measured -19.2 mV

Cell Lines

The A549 human alveolar epithelial adenocarcinoma cell line was supplied from ATCC (CCL-185) and grown in F12-K media supplemented with 10% v/v fetal bovine serum (FBS) and 1% v/v penicillin/streptomycin (Gibco, Invitrogen). The NL20 human bronchial epithelial cell line was supplied from ATCC (NCI-PBCF-CRL2503) and grown in F12-K media supplemented with 4% v/v FBS and 1% v/v penicillin/streptomycin (Gibco, Invitrogen) alongside additional insulin (0.005 mg/mL), epidermal growth factor (10 ng/mL), transferrin (0.001 mg/mL), and hydrocortisone (500 ng/mL). The stable ACE2/TMPRSS-expressing human embryonic kidney HEK293 cell line was kindly provided by Dr. Marc Johnson lab (University of Missouri School of Medicine) and grown in DMEM media supplemented with 10% v/v FBS and 1% v/v penicillin/streptomycin (Gibco, Invitrogen). All cells were grown in 75 cm^2 cell culture flasks (Falcon, Corning) incubated at 37°C and 5% CO_2 in a humidified Heracell VIOS 160i incubator (ThermoFisher Scientific).

Cell Viability

Cells were seeded onto 96-well flat-bottom, tissue culture-treated plate (Falcon) at a density of 5000 cells/well and incubated for 24 h. The cells were then treated with varying concentrations of ACE2-docking filaments (20:1 molar ratio of Filler:Ligand, in 1×PBS at pH = 7.4), ranging from 0.1 to 100 μM, and then incubated for an additional 48 h. Cell viability was assessed with an MTT assay (Invitrogen) according to the manufacturer's protocols. Experiments were performed with 5 technical repeats for each condition with a total of 3 biological repeats.

In Vivo Imaging System (IVIS) Fluorescence Imaging

To execute the imaging, mice were anesthetized with ketamine/xylazine, and given Cy5.5-loaded filaments through nasal inhalation. 24 hour-post inhalations, mice were sacrificed and their whole lungs were isolated. The lung fluorescence image was performed in the IVIS 100 system for 2-5 min at high sensitivity. Regions of interest was identified and quantified using Living Image software (Caliper).

Supplemental References

1. Woody, R.W. (1974). In Peptides, polypeptides and proteins, E.R. Blout, F.A. Bovey, M. Goodman, and N. Lotan, eds. (John Wiley & Sons, Inc.), pp. 338-348.
2. Brahms, S., Brahms, J., Spach, G., and Brack, A. (1977). Identification of β,β-turns and unordered conformations in polypeptide chains by vacuum ultraviolet circular dichroism. Proceedings of the National Academy of Sciences *74*, 3208-3212. 10.1073/pnas.74.8.3208.
3. Brain, J.D., Knudson, D.E., Sorokin, S.P., and Davis, M.A. (1976). Pulmonary distribution of particles given by intratracheal instillation or by aerosol inhalation. Environmental Research *11*, 13-33. 10.1016/0013-9351(76)90107-9.
4. Silva, R.M., Doudrick, K., Franzi, L.M., TeeSy, C., Anderson, D.S., Wu, Z., Mitra, S., Vu, V., Dutrow, G., Evans, J.E., et al. (2014). Instillation versus Inhalation of Multiwalled Carbon Nanotubes: Exposure-Related Health Effects, Clearance, and the Role of Particle Characteristics. ACS Nano *8*, 8911-8931. 10.1021/nn503887r.
5. Leong, B.K.J., Coombs, J.K., Sabaitis, C.P., Rop, D.A., and Aaron, C.S. (1998). Quantitative morphometric analysis of pulmonary deposition of aerosol particles inhaled via intratracheal nebulization, intratracheal instillation or nose-only inhalation in rats. Journal of Applied Toxicology *18*, 149-160. 10.1002/(SICI)1099-1263(199803/04)18:2<149::AID-JAT490>3.0.CO;2-L.
6. Cheetham, A.G., Zhang, P., Lin, Y.-a., Lock, L.L., and Cui, H. (2013). Supramolecular Nanostructures Formed by Anticancer Drug Assembly. Journal of the American Chemical Society *135*, 2907-2910. 10.1021/ja3115983.
7. Su, H., Wang, F., Wang, Y., Cheetham, A.G., and Cui, H. (2019). Macrocyclization of a Class of Camptothecin Analogues into Tubular Supramolecular Polymers. Journal of the American Chemical Society *141*, 17107-17111. 10.1021/jacs.9b09848.
8. Wang, F., Su, H., Lin, R., Chakroun, R.W., Monroe, M.K., Wang, Z., Porter, M., and Cui, H. (2020). Supramolecular Tubustecan Hydrogel as Chemotherapeutic Carrier to Improve Tumor Penetration and Local Treatment Efficacy. ACS Nano *14*, 10083-10094. 10.1021/acsnano.0c03286.
9. Tantakitti, F., Boekhoven, J., Wang, X., Kazantsev, R.V., Yu, T., Li, J., Zhuang, E., Zandi, R., Ortony, J.H., Newcomb, C.J., et al. (2016). Energy landscapes and functions of supramolecular systems. Nature Materials *15*, 469-476. 10.1038/nmat4538.
10. Chen, C.H., Palmer, L.C., and Stupp, S.I. (2018). Self-Repair of Structure and Bioactivity in a Supramolecular Nanostructure. Nano Letters *18*, 6832-6841. 10.1021/acs.nanolett.8b02709.